*Electron. Mater. Lett., Vol. 12, No. 3 (2016), pp. 411-418*
DOI: 10.1007/s13391-016-5391-z

# Polarity-enhanced Gas-Sensing Performance of Au-Loaded ZnO Nanospindles Synthesized via Precipitation and Microwave Irradiation

**Yan Li,* Tan Lv, Fang-Xian Zhao, Xiao-Xue Lian, Yun-Ling Zou, and Qiong Wang**

College of Science, Civil Aviation University of China, Tianjin 300300, PR China

(received date: 26 October 2015 / accepted date: 22 February 2015 / published date: 10 May 2016)

Loading noble metal and exploring suitable morphology to achieve excellent gas-sensing performance is very crucial for the fabrication of gas sensors. We have successfully synthesized Au-loaded ZnO (Au/ZnO) nanospindles (NSs) through a really facile procedure involving a precipitation and subsequent microwave irradiation. The as-prepared products have been characterized by X-ray diffraction (XRD), scanning electron microscope (SEM). The formation and gas-sensing mechanism of Au/ZnO NSs were discussed. The SEM micrographs revealed an interesting morphological evolution of the Au/ZnO NSs with Au-loading content ranging from 0 at. % to 7 at. %. The nanostructures were employed for gas-sensing measurement toward various gases. It indicated that the Au/ZnO NSs based sensor showed a highly enhanced response (226.81) to 400 ppm acetone gas at a relatively low working temperature (270°C), and exhibited a fast response (1 s) and recovery speed (10 s). The highly enhanced acetone gas sensitivity of Au/ZnO NSs based sensor could be attributed to its enhanced polarity owing to the peculiar morphology, Schottcky barriers, as well as catalytic effect of Au NPs.

**Keywords:** zinc oxide, Au modification, acetone sensor, gas sensing, nanospindle, mechanism

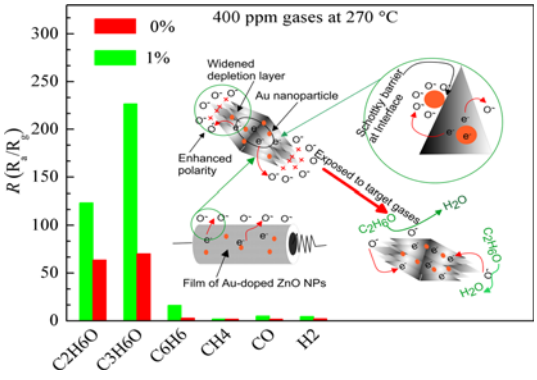


## 1. INTRODUCTION

In recent years, much crucial demands for development of security monitoring and detection technologies have been exponentially increasing because of dangerous gases extensively used in industries and daily life.[1-3] Therefore, gas-sensing technologies and its relative materials were considered to be the most critical issue to prevent lives and property from their potentially dangerous environments and working conditions. In the past decades, solid-state gas sensors have been widely investigated and used in applications for monitoring the environmental and chemical process, occupational health and safety, and medical devices.[4-6] As one of solid-state materials, semiconductor metal oxide has attracted much more attention due to low cost, fast response and recovery, and high compatibility. A great number of semiconductor metal oxides such as ZnO, $SnO_2$, $WO_3$, $TiO_2$, and $V_2O_5$ based gas sensors have been fabricated and investigated.[7-12] Among the above oxides, ZnO, with a large exciton binding energy (60 meV), a wide band gap (3.37 eV) and the richest morphologies, is well considered an very important functional material due to many efficient applications of gas sensors, solar cells, photocatalysis, piezoelectric transducers. Many researches revealed that the morphologies and chemical composition of semiconductor materials always play a radical role to adjust the gas-sensing performance.[13-15] Hence, many peculiar ZnO with different morphologies, such as nanorods, nanospindles, nanosheets, nanofiber, nanobelts, nanotubes, nanowire and hollow nanospheres[16-21] have been synthesized via various fabrication methods that including

*Corresponding author: liyan01898@163.com

chemical precipitation, hydrothermal crystallization, chemical vapor deposition, physical vapor deposition, and solid-state phase transition.[22-25] Monodispersed ZnO hollow microspheres were synthesized through a glycerol-mediated hydrothermal route, the sensor based on the hollow spheres exhibited high response and good selectivity to ethanol at 380°C.[26] On the other hand, loading noble metal is considered a very effective way for improving the gas-sensing properties.[27] Li-loaded ZnO nanoparticles with a high sensitivity and selectivity toward 100 ppm methanol and formaldehyde were hydrothermally synthesized.[28] Phan *et al.*[29] reported a Ga-loaded ZnO nanorods hydrothermally synthesized showed an enhanced sensing to CO at a relatively low temperature (150°C). It is proven that Au-loading can significantly improve the sensitivity and selectivity of ZnO nanostructures to various gases.[30-33] Although some great efforts have been paid for development of Au-loaded ZnO nanostructure and achieved a lot of highly sensitive Au/ZnO, it is still necessary to further improve the response and decrease the operating temperature for application in high level.

In this work, we report an Au-loaded ZnO NSs fabricated via an extremely facile and quick method just including precipitation and microwave irradiation process. The growth and gas-sensing mechanism of the Au/ZnO NSs were discussed. The as-prepared Au/ZnO NSs exhibited a higher response (226.81) to 400 ppm acetone gas at a relative low temperature (270°C).

## 2. EXPERIMENTAL PROCEDURE

### 2.1 Experimental

Au-loaded ZnO NSs were synthesized according to the following process. 0.01 mol/L zinc nitrate ($Zn(NO_3)_2 \cdot 6H_2O$, A.R., 98%), 0.01 mol/L sodium hydroxide (NaOH (A.R., 96%) and 0.012 mol/L auric chloride acid ($HAuCl_4$, A.R., Au > 47%) solutions were prepared respectively. The sodium hydroxide solution was dropwise added into the zinc nitrate solution, then auric chloride acid solution and a certain sodium citrate as a reducer were added into the mixture solution, under a magnetic stirring at 2,000 rpm for 2 h at 60°C. After that, we centrifugally washed the precipitate many times with distilled water and ethanol ($C_2H_5OH$, A.R., >99.7%) respectively at 10,000 rpm to wash off any impurities. Then the wet centrifuged products were irradiated under microwave field with a power of 700 W to obtain the ultimate products. Au-loading content (Au(mol)/Zn(mol)) adopted in this experiment was 0%, 0.25%, 0.5%, 1%, 3%, 5%, and 7%, respectively.

The crystal structure was characterized by a DX-2000 X ray diffractometer (Dandong Fang-Yuan Instrument Co., Ltd.) operating at 40 kV and 25 mA using Cu Kα ($\lambda$ = 0.154184 nm) radiation source employing a scanning rate

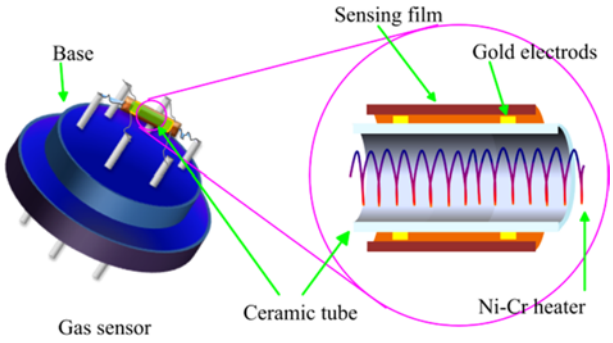


**Fig. 1.** Schematic diagram of a typical gas sensor.

0.05 deg./s with 2θ ranging from 30 to 70 deg.. Field emission scanning electron microscopy (FE-SEM, Hitachi X-650) and transmission electron microscopy (Hitachi HT7700) were used to investigate the morphology and energy dispersive spectroscopy (EDS) of the samples. The Hitachi F-7000 spectrometer was used to record the photoluminescence (PL) spectrum with 325 nm as the excitation wavelength.

The fabrication procedures of gas sensor have been described in literature elsewhere,[27] and described in Fig. 1. A dilute slurry composed of the as-prepared NPs and deionized water was coated onto an alumina tube with a diameter of 1 mm and a length of 4 mm, being positioned with a pair of Au electrodes and four Pt wires on both ends of the tube. A Ni-Cr alloy coil through the tube was employed as a heater to control the operating temperature. Subsequently the gas sensors were dried in shade at room temperature for 24 h, subsequently anchored in an aging device at 80 mA for 24 h, following 180 mA for 3 h to get a quick heater-type ZnO gas sensor. The gas sensing property was measured with a chemical gas sensor-8 intelligent gas sensing analysis system (Beijing Elite Tech Co., Ltd., China) after the fabricated gas sensors sintered for 48 h under 80 mA. The gas sensitivity (S) was defined as $R = Ra/Rg$, where $Ra$ and $Rg$ are sensor resistance in the air and target gas.

## 3. RESULTS AND DISCUSSION

### 3.1 XRD and FE-SEM investigation

Figure 2 presents the XRD patterns of the main crystal phases of the as-obtained Au/ZnO nanoparticles. For all samples, diffraction peaks (100), (002), (101), (102), (110), (103), and (112) are observed at 31.78°, 34.54°, 36.36°, 47.69°, 56.76°, 62.90°, and 68.13°, respectively, indicating a hexagonal wurtzite ZnO structure (JCPDS Card No.36-1451). It can be found that the full-width at half-maximum of all peaks of Au/ZnO increase and the intensities decrease with increasing Au-loading content, indicating the inhibited

effect of Au-loading on the grain growth of ZnO. We noted that upon increasing the amount of Au-loading, no any characteristic peaks of Au metal crystal phase could be observed in these XRD patterns. But FE-SEM image and EDS results revealed that Au nanoparticles effectively exist in these samples. It implies that Au nanoparticles are in the

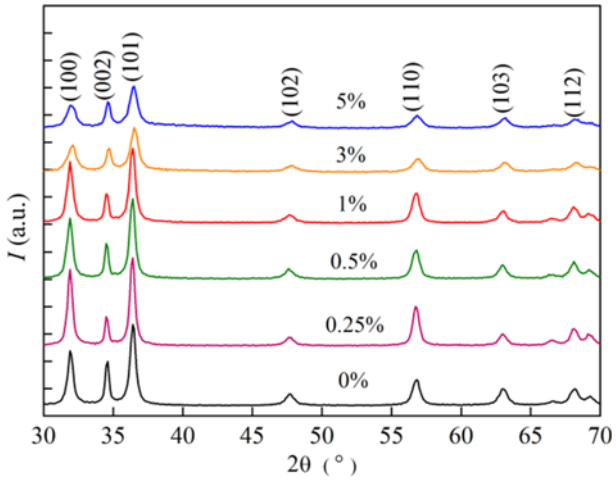


**Fig. 2.** XRD patterns of Au-loaded ZnO NPs with different Au-loading of 0 at. % (a), 0.25 at. %, 0.5 at. %, 1 at. %, 3 at. %, and 5 at. %.

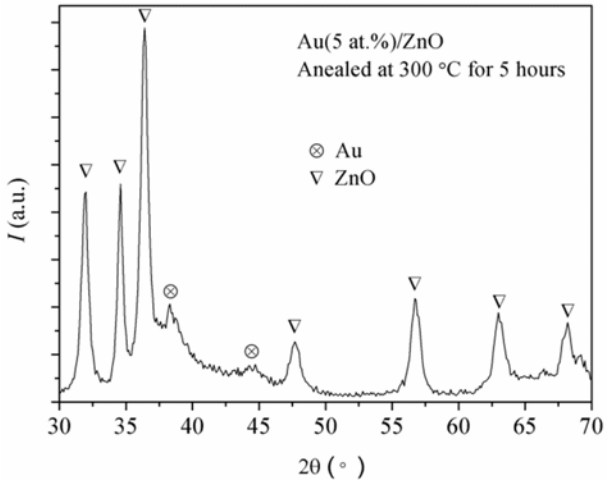


**Fig. 3.** XRD pattern of the annealed Au(5 at. %)/ZnO NSs at 300°C for 5 h.

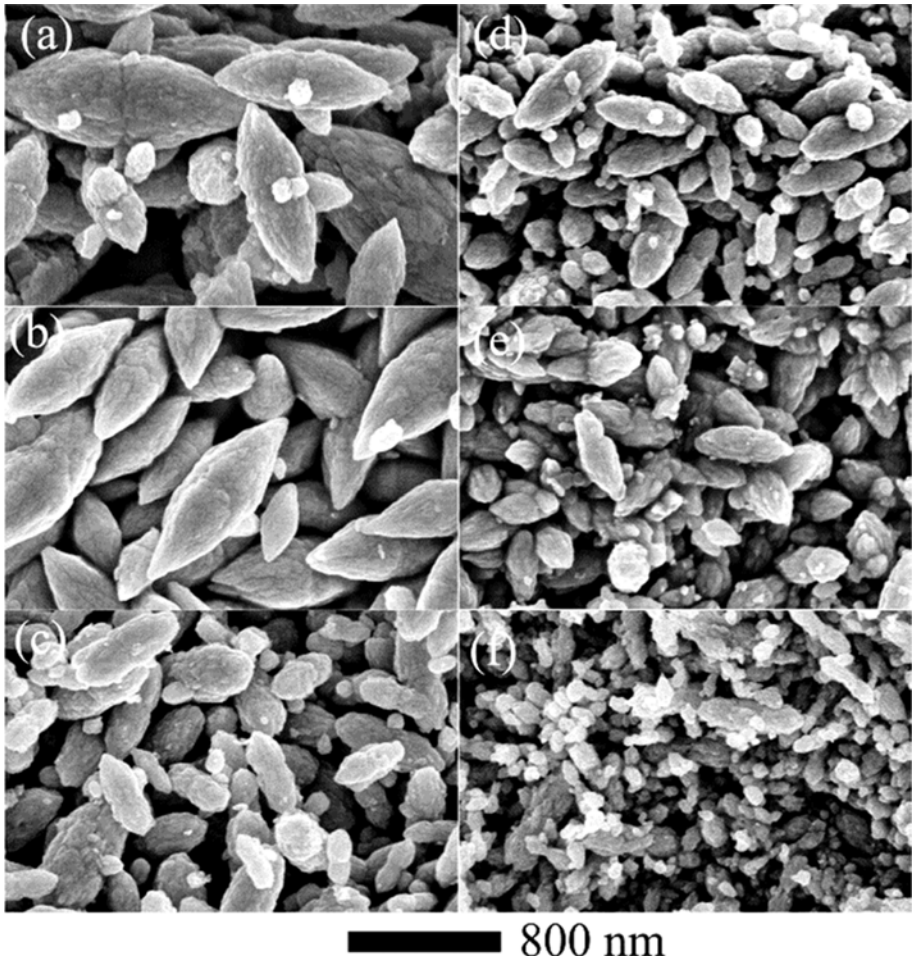


**Fig. 4.** FE-SEM images of Au-loaded ZnO NPs with different Au-loading of 0 at. % (a), 0.25 at. %, 0.5 at. %, 1 at. %, 3 at. %, and 5 at. %.

amorphous state. In order to further prove this issue, the Au/ZnO loaded with 5 at. % of Au was annealed at 300°C for 5 h, which then was characterized by XRD (Fig. 3). The XRD pattern shows that peaks relate to (111) and (200) planes are clearly observed at 38.17° and 44.39°, which correspond well to face-centered cubic crystalline Au (JCPDS Card No. 04-0784). This can be attributed to the following reasons. As the precursor is placed in microwave field, irradiation energy is almost consumed by the crystallization and oriented growth of ZnO NPs, and Au NPs can't absorb any microwave irradiation to evaluate its temperature enough for crystallization.

Figure 4 shows the morphologies of Au/ZnO NSs loaded with different Au/Zn ratio. It can be clearly observed that the unloaded ZnO appears a spindle-like shape with a length of ~800 nm (Fig. 4a). With a close watch, the scraggly spindles are composed of two prisms built of numerous nanoparticles in diameters of 50 - 70 nm. The size of Au/ZnO NSs gradually become smaller and their surface appears more rough when increasing Au-loading content in the range from 0 to 3 at. %. We note that the Au(5 at. %)/ZnO is no longer a spindle-like shape, just numerous nanoparticles with diameters of 50 - 70 nm, and it is in the same dimension with the nanoparticles in pure ZnO spindles. It implies that the spindle morphology can't form as Au-loading content more than a certain value (5 at. %), and Au nanoparticles locates in the interface of ZnO nano-units inhibit the spindle formation. Interestingly, the Au(1 at. %) /ZnO has the highest response, according to the following gas-sensing results (Fig. 7 and Fig. 8), and it embodies characteristics, including the smaller size, the most surface roughness, and the critical content of Au-modification that didn't destroy the spindle structure. The EDS results are shown in Fig. 5, indicating the sample Au(7 at. %)/ZnO has an Au/Zn ratio of 9.3 more than the Au/Zn ratio employed in experimental

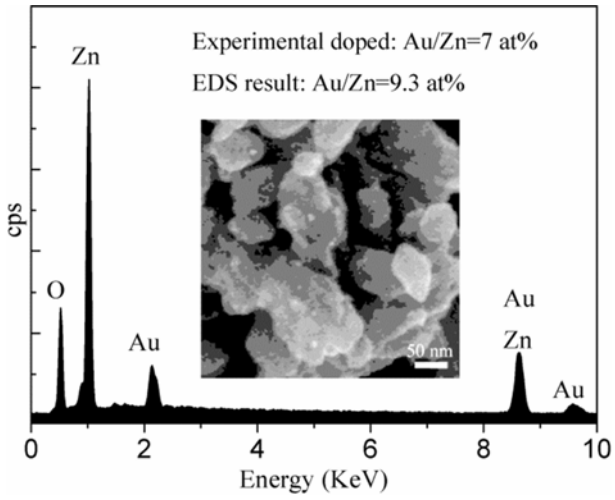


**Fig. 5.** EDS data and FE-SEM image of Au(7 at. %)/ZnO NPs.

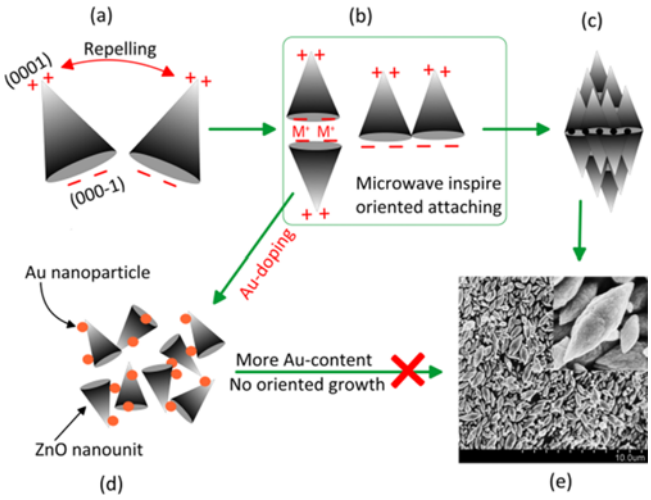


**Fig. 6.** Schematic diagram of the oriented growth mechanism of spindle-shaped ZnO NPs.

because more Au nanoparticles locate on the surface of ZnO particles (the inset image in Fig. 5).

Based on the above analysis, the reasonable growth mechanism of the ZnO NSs is proposed as follows. Due to the polarity of ZnO nano-units (the tiny prisms in Fig. 6a), the top (0001) plane of these prisms tends to repel each other since the surface of the tops exposes a certain positive charge. In contrast, the (000-1) planes attracting each other through absorbing other cations ($M^+$). In general synthesis system (e.g. hydrothermal system), these prisms can't orderly assemble to spindle morphology because the crowded place between prisms inhibits the repelling and attracting action. Under microwave irradiation, the electronic field force boosts the vibration, repelling and attracting action, which make these prisms arranged in an orderly state (Fig. 6b) to form spindle morphology (Fig. 6c and 6e). Furthermore, this spindle exposes more polar planes to enhance the polarity that can absorb more oxygen atoms in air, which take benefits for gas-sensing. When excess Au loaded in ZnO, Au nanoparticles can hinder the oriented growth behavior, not to form spindle shapes (Fig. 6d).

### 3.2 Analysis of gas-sensing performance

Many relative researches have proven that the response of metal oxide semiconductor gas sensors mainly depend on the operating temperature. Therefore, it is necessary to investigate the optimum operating temperature of all the prepared sensor devices. Both the sensors such as pure ZnO and Au/ZnO NSs were tested at different temperatures from 180 to 420°C for 50 ppm of acetone gas, the results of which are shown in Fig. 7. It can be seen that the sensing responses of all samples increase and then decreases with operating temperature increasing. It indicates that the Au/ZnO sensors have same gas-sensing process of semiconductor materials

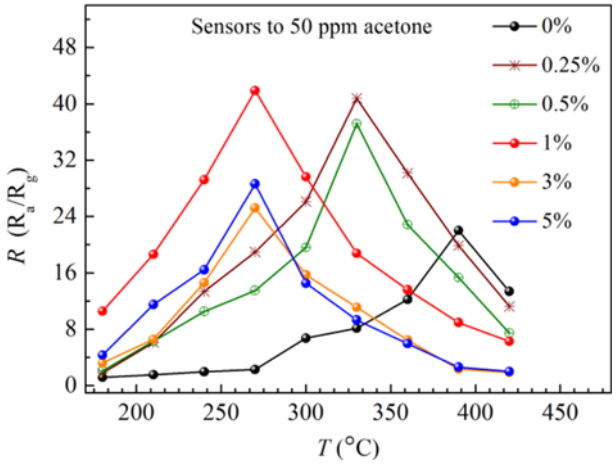


**Fig. 7.** Responses (*R*) of Au-loaded ZnO NPs with different Au-loading of 0 at. % (a), 0.25 at. %, 0.5 at. %, 1 at. %, 3 at. %, and 5 at. % versus working temperature (*T*).

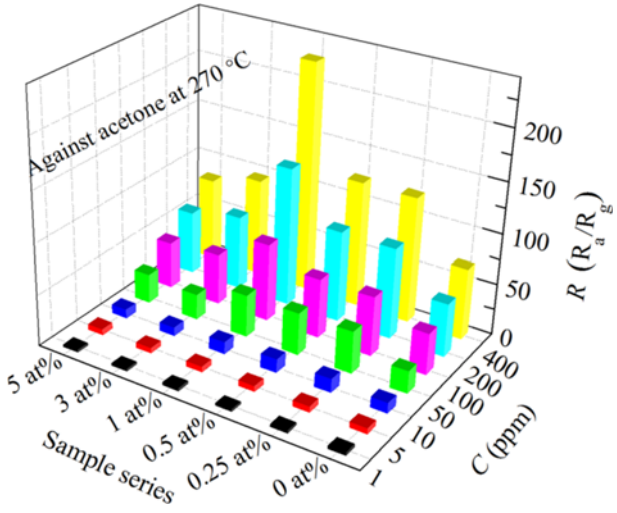


**Fig. 8.** Histogram of the response (*R*) versus gas concentration (*C*) that relate to Au-loaded ZnO NPs with different Au-loading of 0 at. % (a), 0.25 at. %, 0.5 at. %, 1 at. %, 3 at. %, and 5 at. %.

involves the adsorption and desorption of gases, and reaction of the adsorbed gases on the surface-active sites of the materials. Sufficiently thermal energy is essential across the activation energy barrier for chemisorption and reaction between adsorbed gases on the surface of materials. The amount of chemical-adsorbed gas molecules increases with the increase of operating temperature, and the higher sensing response is obtained. However, as the operating temperature further increases, the desorption process becomes dominant, resulting in the decrease of the response. Comparing with these curves, we can find that the unloaded ZnO has a relatively high operating temperature (390°C) and low response (22). With increasing Au-loading content, the response increases and the working temperature obviously decreases until Au-loading of 3 at. %. The Au(1 at. %)/ZnO spindles have the highest response (42) to 50 ppm acetone gas and the lowest working temperature (270°C) among all the as-synthesized samples. Therefore, the temperature (270°C) is taken as the optimal working temperature of the Au/ZnO nanoparticles in this work to be used in the following gas-sensing measurement.

Figure 8 shows the response comparison histogram between the sample series that loaded Au with concentrations of 0 - 5 at. % against different acetone concentration ranging from 1 ppm to 400 ppm. It can be clearly seen that the response of Au(1 at. %)/ZnO has the highest response among all samples at each gas concentration.

To compare the sensor responses to acetone versus other gases, the responses of pure ZnO and Au(1 at. %)/ZnO toward benzene ($C_6H_6$), hydrogen ($H_2$), acetone ($C_3H_6O$), ethanol ($C_2H_5OH$), carbon monoxide (CO), and methane ($CH_4$) at 270°C are shown in Fig. 9. Both the pure ZnO and Au(1 at. %)/ZnO are clearly more sensitive to acetone than other gases ($C_6H_6$, $C_2H_5OH$, $H_2$, CO, and $CH_4$), and the

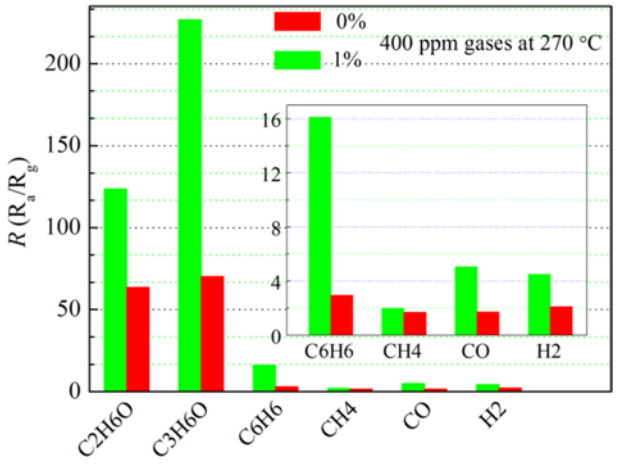


**Fig. 9.** Responses (*R*) of Au(0 at. %)/ZnO and Au(1 at. %)/ZnO to different target gases with concentration (*C*) of 400 ppm at 270°C.

response of the sensor made from Au(1 at. %)/ZnO to acetone is approximately 8.4 times greater than that of the pure ZnO. Furthermore, the response of the sensor made from Au(1 at. %)/ZnO to acetone (226.5) is higher more than that of $C_2H_5OH$, $C_6H_6$, $CH_4$, CO, and $H_2$. The responses of the sensor to the above gases are in order of $C_3H_6O$ > $C_2H_6O$ > $C_6H_6$ > CO > $H_2$ > $CH_4$.

Figure 10 shows the responses of the pure ZnO and Au(1 at. %)/ZnO versus acetone at different concentration. We can find that there is no obvious difference between the responses of the pure ZnO and Au(1 at. %)/ZnO at low acetone concentration, but the response of Au(1 at. %)/ZnO quickly increases with increasing acetone concentration in a large scale. The responses of the Au(1 at. %)/ZnO based sensor are 7, 9.4, 14.4, 42.8, 76.5, 136.4, and 226.8 toward

acetone gas with different concentrations of 1 ppm, 5 ppm, 10 pp, 20 ppm, 50 ppm, 100 ppm, 200 ppm and 400 ppm, respectively. It implies the Au(1 at. %)/ZnO based sensor has no adsorption saturation to target gases, which very benefits the gas-sensing improvement. In comparison with the newly reported Au@ZnO yolk shell nanospheres (37 to 100 ppm acetone),[34] indicating a highly enhanced gas sensing performance. The response of the Au(1 at. %)/ZnO based sensor toward 400 ppm acetone is significantly higher (226.8) in comparison with the pure ZnO based sensor (91), indicating remarkable enhancement of Au-loading onto pure ZnO for the gas-sensing performance. The inset in Fig. 10 shows the response and recovery time of the Au(1 at. %)/ZnO against 400 ppm acetone at 270°C are 1 s and 10 s as marked in the graph, respectively. The reliability test of the Au(1 at. %)/ZnO based sensor was carried out at 270°C against 400 ppm acetone. Figure 11 shows no any decay of the response even after seven cycle tests, promising an excellent reliability. A comparison of the gas sensing performance between several previously reported binary metal/ZnO hybrids based sensors and the Au/ZnO NSs based sensor is summarized in Table 1. The Au/ZnO NSs based sensor in this work apparently exhibits a highly enhanced gas-sensing performance.

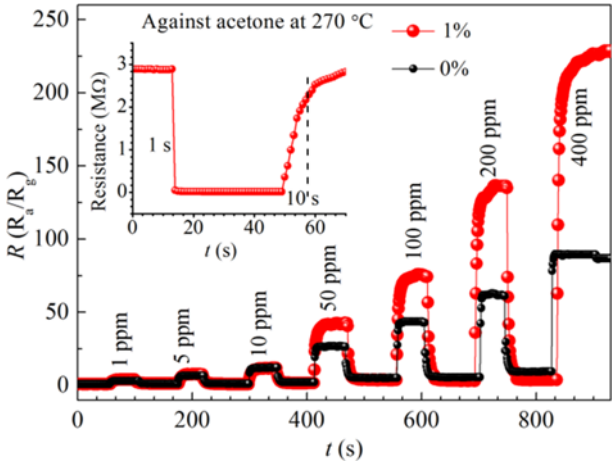


**Fig. 10.** Responses (*R*) of Au(0 at. %)/ZnO and Au(1 at. %)/ZnO versus acetone concentration (*C*) at 270°C; the inset is the resistance curve of Au(1 at. %)/ZnO versus time (*t*).

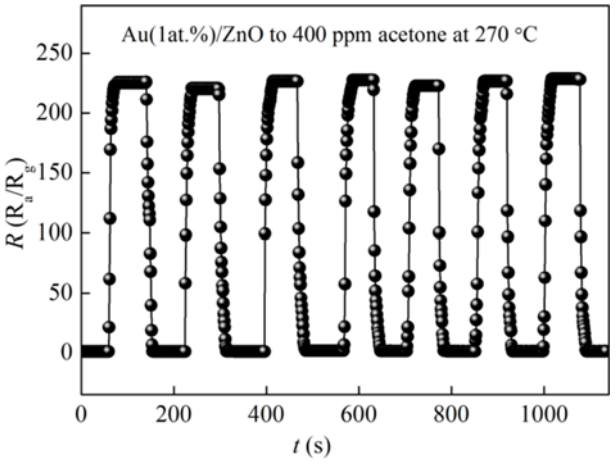


**Fig. 11.** Cycle test of the sensing performance of Au(1 at. %)/ZnO to 400 ppm acetone at 270°C.

**Table 1.** Comparison of acetone sensing performance between this work and some previous works.[34-39]

| Materials | *C* (ppm) | *T* (°C) | *R* | $R_s/R_c$ | Refs |
|---|---|---|---|---|---|
| Au/ZnO | 400 | 270 | 226.8 | 1/10 s | This work |
| Au/ZnO | 500 | 300 | 140 | 2/38 s | [33] |
| Au/ZnO | 200 | 325 | 2 | - | [34] |
| Pd/ZnO | 500 | 340 | 222 | 9/6 s | [35] |
| Ce/ZnO | 500 | 230 | 71.2 | 8/5 s | [36] |
| $La_2O_3$/Zn | 200 | 350 | 54.1 | 11/17 s | [37] |
| ZnO flower | 500 | 250 | 4 | - | [38] |

*C*-Acetone concentration; *T*-Working temperature; *R*-Response; *Rs*-Response time; *Rc*-Recovery time

### 3.3 Gas-sensing mechanism

Based on the above results and analysis, a brief and reasonable gas-sensing mechanism of Au-loaded ZnO NSs is described as following. It is well known that when sensors are exposed to air, the surface of the ZnO NSs adsorbs atmospheric oxygen, and the adsorbed oxygen captures electrons from the conduction band of the ZnO to produce oxygen ions ($O^-$ or $O_2^-$). The reaction mechanism is as follows.[40]

$$O_{2\,(ads.)} + 2e^- \rightarrow 2O^-_{\,(ads.)} \quad (1)$$

$$O_{2\,(ads.)} + e^- \rightarrow O_2^-{}_{\,(ads.)} \quad (2)$$

This forms depletion layer in surface of ZnO NSs, causing decrement in carrier concentration (Fig. 12b). Therefore, resistance of ZnO in ambient air is higher than that in vacuum. In this work, the spindle morphology plays a rather crucial role for improving the gas-sensing performance. As shown in Fig. 12b, science the spindles are made of many tiny polar ZnO nanoprisms in a highly order structure, the polarity of the both ends of the spindles is significantly enhanced, which devotes more positive effect on adsorbing more oxygen atoms when the sensor exposed in air. This result causes the depletion layer of the spindles widened (Fig. 12b), and more electronic transformation when the sensor exposed from air to target gases. Moreover, the out surfaces of these spindles appear more positively charged polar planes while the negatively charged (000-1) planes hide under the surface of the spindles. This makes the amount of the absorbed oxygen atoms further increases. In addition, Au-loading unavoidably causes a new interface

occurs between Au nanoparticles and bulk ZnO. At the same time, Au can also provide a chemical mechanism for the depletion of electrons on the ZnO surface, Au nanoparticles catalytically activate the adsorption and dissociation of molecular oxygen on the surface of the ZnO, in which oxygen molecules capture free electrons from the ZnO and form oxygen ions ($O_2^-$).[31] When acetone is introduced at operating temperature, the acetone molecules will react with adsorbed $O^-$ or $O_2^-$, releasing trapped electrons back to conduction band to narrow the depletion layer until its disappearance, and therefore the conductivity of the ZnO sensors increases.[41] This principle plays a crucial role for enhancement of gas sensing performance. The higher acetone selectivity and response can be explained by comparison of the following reaction equations (Eq.) between different target gas molecules and $O^-$, which is described as follows.

$$C_3H_6O + O^- \rightarrow 3CO_2 + 3H_2O + 8e^- \quad (3)$$
$$C_2H_6O + 6O^- \rightarrow 2CO_2 + 3H_2O + 6e^- \quad (4)$$
$$C_6H_6 + 15O^- \rightarrow 6CO_2 + 3H_2O + 15e^- \quad (5)$$
$$H_2 + O^- \rightarrow H_2O + e^- \quad (6)$$
$$CO + O^- \rightarrow CO_2 + e^- \quad (7)$$
$$CH_4 + 4O^- \rightarrow CO_2 + 2H_2O + 4e^- \quad (8)$$

According to reaction Eq. (3) to (8), the electrons donating ability is in order of $C_6H_6 > C_3H_6O > C_2H_6O > CH_4 > H_2$ and CO. This order apparently can't match the above gas-sensing results. The number of actually released electrons from reaction between target gases and $O^-$ depends on the electron donating ability, as well as mainly lies on the adsorption behavior of target gases onto the surface of ZnO NSs. Science the as-prepared Au/ZnO NSs exhibits strong polarity, the target gas polarity is a very important factor for adsorption behavior. The dipole moment ($\mu$/D) of these target gases are in order of $C_3H_6O$ (2.88) > $C_2H_6O$ (1.69) > $C_6H_6$ (0), CO(0.11), $H_2$ (0), and $CH_4$ (0), which is completely identical with the experimental results. Acetone molecule with the maximum polarity among the above gases is easily adsorbed onto or desorbed from the polar surface of ZnO NSs, so the gas-sensing response to acetone is higher than that to other gases.

Moreover, the ratio ($R_c/w$) of the radius ($R_c$) of ZnO to the width ($w$) of depletion layer significantly affects the sensing response. With decreasing $R_c/w$, the response will increase.[42] The as-prepared Au/ZnO NSs consists of numerous nanoparticles just in range of 20 - 40 nm in spite of the spindles having a relatively larger length of 200 - 800 nm, with a very small $R_c/w$, which beneficial to sensing response. Because of the work function of ZnO (~5.3 eV) is slightly lower than that of Au (~5.47 eV) and therefore its Fermi energy level is higher than that of Au,[43] so electrons will flow from ZnO to Au NPs, to ensure similar Fermi energy levels between the two materials. This subsequently creates

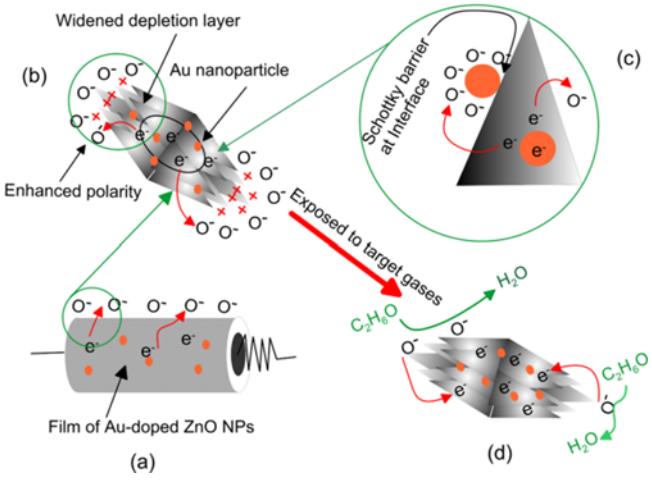


**Fig. 12.** Gas-sensing mechanism of the sensor based on the Au-loaded ZnO nano-spindles.

a Schottky barrier at the Au/ZnO heterojunction interface,[44,45] which leads to relatively wide width of the depletion layer of ZnO (Fig. 12b). Above all, the excellent sensing performance of Au/ZnO NPs can be attributed to the combination of the polarity-enhanced spindle morphology, Schottky barrier, and Au catalysis.

## 4. CONCLUSIONS

Au-loaded ZnO spindles with higher response and a low working temperature toward acetone were synthesized using a facile and effective approach just including a precipitation and microwave irradiation process. The proposed synthesis method is advantageous because of its really simple procedures. The spindle morphology is due to orderly attaching growth of polarized ZnO nanoprisms. The gas-sensing performance mainly depends on the spindle polarity and Au-loading. The enhanced response of Au/ZnO NPs can be attributed to the combination of the spindle morphology, Schottky barrier, and Au catalyst. The facile preparation and excellent sensing properties of the Au/ZnO spindles suggest their potential in acetone-sensor-related practical applications.

## ACKNOWLEDGEMENTS

This research was mainly supported by the Fundamental Research Funds for the Central Universities (No. 3122013k007), and the Science and Technology Innovation Guide Funds of Civil Aviation Administration of China (No. MHRD20140209).

## REFERENCES

1. X. X. Yu, X. S. Liu, M. Z. Wu, Z. Q. Sun, G. Li, and X. S. Chen, *Chinese J. Chem. Phys.* **27**, 99 (2014).
2. V. Talwar, O. Singh, and R. C. Singh, *Sensor Actuat. B-*

*Chem.* **191**, 276 (2014).
3. G. Korotcenkov, L. B. Gulina, B. K. Cho, S. H. Han, and V. P. Tolstoy, *Mater. Chem. Phys.* **128**, 433 (2011).
4. Y. M. Zhu, V. Thangadurai, and W. Weppner, *Sensor Actuat. B-Chem.* **176**, 284 (2013).
5. B. C. Yadav, A. Yadav, T. Shukla, and S. Singh, *B Mater. Sci.* **34**, 1639 (2011).
6. J. Herran, O. Fernandez-Gonzalez, I. Castro-Hurtado, T. Romero, G. G. Mandayo, and E. Castano, *Sensor Actuat. B-Chem*. **149**, 368 (2010).
7. D. Zhu, T. X. Hu, Y. Y. Zhao, W. L. Zang, L. L. Xing, and X. Y. Xue, *Sensor Actuat. B-Chem.* **213**, 382 (2015).
8. Q. Q. Zhao, D. X. Ju, X. L. Deng, J. Z. Huang, B. Q. Cao, and X. J. Xu, *Sci. Rep.-Uk* **5** (2015).
9. L. Yin, D. L. Chen, H. W. Zhang, G. Shao, B. B. Fan, R. Zhang, and G. S. Shao, *Mater. Chem. Phys.* **148**, 1099 (2014).
10. Y. Yang, C. G. Tian, J. C. Wang, L. Sun, K. Y. Shi, W. Zhou, and H. G. Fu, *Nanoscale* **6**, 7369 (2014).
11. R. J. Wu and T. M. Wu, *Sensor Lett*. **8**, 564 (2010).
12. P. D. Burton, D. Lavenson, M. Johnson, D. Gorm, A. M. Karim, T. Conant, A. K. Datye, B. A. Hernandez-Sanchez, and T. J. Boyle, *Top Catal* **49**, 227 (2008).
13. Y. S. Wang, S. R. Wang, H. X. Zhang, X. L. Gao, J. D. Yang, and L. W. Wang, *J. Mater. Chem. A* **2**, 7935 (2014).
14. D. Barreca, E. Comini, A. P. Ferrucci, A. Gasparotto, C. Maccato, C. Maragno, G. Sberveglieri, and E. Tondello, *Chem. Mater.* **19**, 5642 (2007).
15. C. Bittencourt, E. Llobet, M. A. P. Silva, R. Landers, L. Nieto, K. O. Vicaro, J. E. Sueiras, J. Calderer, and X. Correig, *Sensor Actuat. B-Chem.* **92**, 67 (2003).
16. Y. Zhang, T. M. Liu, H. Zhang, W. Zeng, F. S. Pan, and X. H. Peng, *J. Mater. Sci.-Mater. El.* **26**, 191 (2015).
17. J. P. Zhang, T. M. Liu, Y. Zhang, W. Zeng, F. S. Pan, and X. H. Peng, *J. Mater. Sci.-Mater. El.* **26**, 1347 (2015).
18. B. W. Yu, Y. M. Fu, P. L. Wang, Y. Y. Zhao, L. L. Xing, and X. Y. Xue, *Phys. Chem. Chem. Phys.* **17**, 10856 (2015).
19. H. Y. Fu, X. Y. Lang, C. Hou, Z. Wen, Y. F. Zhu, M. Zhao, J. C. Li, W. T. Zheng, Y. B. Liu, and Q. Jiang, *J. Mater. Chem. C* **2**, 7216 (2014).
20. R. C. Pawar, J. S. Shaikh, S. S. Suryavanshi, and P. S. Patil, *Curr. Appl. Phys.* **12**, 778 (2012).
21. Y. Li, D. L. Li, and J. C. Liu, *Chinese Chem. Lett*. **26**, 304 (2015).
22. X. H. Jia, H. Q. Fan, M. Afzaal, X. Y. Wu, and P. O'Brien, *J. Hazard. Mater*. **193**, 194 (2011).
23. R. Garcia-Gutierrez, M. Barboza-Flores, D. Berman-Mendoza, R. Rangel-Segura, and O. E. Contreras-Lopez, *Adv. Mater. Sci. Eng.* **2012**, 5 (2012).
24. D. W. Zhang, X. F. Wu, N. Han, and Y. F. Chen, *J. Nanopart Res.* **15**, 1580 (2013).
25. J. J. Zhang, E. J. Guo, H. Y. Yue, L. P. Wang, C. Y. Zhang, J. Chang, and X. Gao, *J. Mater. Sci.-Mater. El.* **24**, 3435 (2013).
26. H. M. Sun, L. M. Wang, D. Q. Chu, Z. C. Ma, A. X. Wang, Y. J. Zheng, and L. D. Wang, *Ceram. Int*. **40**, 16465 (2014).
27. Y. C. Liang, W. K. Liao, and X. S. Deng, *J. Alloy Compd.* **599**, 87 (2014).
28. J. W. Zhao, C. S. Xie, L. Yang, S. P. Zhang, G. Z. Zhang, and Z. M. CaiState, *Appl. Surf. Sci*. **330**, 126 (2015).
29. D. T. Phan and G. S. Chung, *Sensor Actuat. B-Chem.* **187**, 191 (2013).
30. L. W. Wang, S. R. Wang, M. J. Xu, X. J. Hu, H. X. Zhang, Y. S. Wang, and W. P. Huang, *Phys. Chem. Chem. Phys.* **15**, 17179 (2013).
31. J. Guo, J. Zhang, M. Zhu, D. X. Ju, H. Y. Xu, and B. Q. Cao, *Sensor Actuat. B-Chem.* **199**, 339 (2014).
32. N. S. Ramgir, P. K. Sharma, N. Datta, M. Kaur, A. K. Debnath, D. K. Aswal, and S. K. Gupta, *Sensor Actuat. B-Chem.* **186**, 718 (2013).
33. Y. Li, T. Lv, F.-X. Zhao, Q. Wang, X.-X. Lian, and Y.-L. Zou, *Electron. Mater. Lett.* **11**, 890 (2015).
34. X. Li, X. Zhou, H. Guo, C. Wang, J. Liu, P. Sun, F. Liu, and G. Lu, *ACS Appl. Mater. Interfaces* **6**, 18661 (2014).
35. X. W. Li, W. Feng, Y. Xiao, P. Sun, X. L. Hu, K. Shimanoe, G. Y. Lu, and N. Yamazoe, *Rsc. Adv.* **4**, 28005 (2014).
36. Y. H. Xiao, L. Z. Lu, A. Q. Zhang, Y. H. Zhang, L. Sun, L. Huo, and F. Li, *Acs Appl. Mater. Inter.* **4**, 3797 (2012).
37. G. X. Wan, S. Y. Ma, X. B. Li, F. M. Li, H. Q. Bian, L. P. Zhang, and W. Q. Li, *Mater. Lett.* **114**, 103 (2014).
38. J. Q. He, J. Yin, D. Liu, L. X. Zhang, F. S. Cai, and L. J. Bie, *Sensor Actuat. B-Chem.* **182**, 170 (2013).
39. Z. S. Hosseini, A. Mortezaali, and A. I. Zad, *Sensor Actuat. A-Phys.* **212**, 80 (2014).
40. R. C. Pawar, J. S. Shaikh, A. V. Moholkar, S. M. Pawar, J. H. Kim, J. Y. Patil, S. S. Suryavanshi, and P. S. Patil, *Sensor Actuat. B-Chem.* **151**, 212 (2010).
41. R. C. Pawar, J. W. Lee, V. B. Patil, and C. S. Lee, *Sensor Actuat. B-Chem.* **187**, 323 (2013).
42. J. Q. Liu, G. H. Jin, Z. X. Zhai, F. F. Monica, and X. S. Liu, *Electron. Mater. Lett.* **11**, 457 (2015).
43. S. Y. Lin, S. J. Chang, and T. J. Hsueh, *Appl. Phys. Lett.* **104**, 5 (2014).
44. S. Ju, S. Kim, S. Mohammadi, D. B. Janes, Y. G. Ha, A. Facchetti, and T. J. Marks, *Appl. Phys. Lett.* **92**, 022104-1-3 (2008).
45. Y. V. Kaneti, J. L. Moriceau, M. Liu, Y. Yuan, Q. Zakaria, X. H. Jiang, and A. B. Yu, *Sensor Actuat. B-Chem.* **209**, 889 (2015).